

# Corrosion Behavior of Novel Mg-9Li-7Al-1Sn and Mg-9Li-5Al-3Sn-1Zn Alloys in NaCl Aqueous Solution

Vinod Kumar, Rajiv Shekhar, and Kantesh Balani

(Submitted April 2, 2015; in revised form July 6, 2015)

Corrosion behavior of two multiphase Mg-Li-Al-based alloys in 0.6 M NaCl aqueous solution is investigated by hydrogen gas evolution measurement and electrochemical test. This paper reports, for the first time, the comparison of hydrogen evolution and Tafel extrapolation results of Mg-Li-Al-based alloys. The corrosion rate of Mg-9Li-7Al-1Sn is observed to be reasonably higher when compared to that of Mg-9Li-5Al-3Sn-1Zn, and both the alloys have shown higher corrosion rate than that of Mg-3Al-1Zn alloy (AZ31B). The micro-galvanic corrosion of primary precipitates and hcp  $\alpha$ -phase (Mg-rich) is not as severe as was observed in case of the secondary precipitates and bcc  $\beta$ -phase (Li-rich). Corrosion mechanism of multiphase Mg-Li-Al-based alloys in chloride solution, which has not been adequately reported in the literature, is lucidly articulated based on the early stages of corrosion, film morphology, and in situ hydrogen bubble study.

**Keywords** characterization, corrosion, hydrogen gas evolution, magnesium

## 1. Introduction

Commercial applications of magnesium-based alloys are promising for aerospace and automobile applications due to their lower density, higher specific strength-to-weight ratio, high specific elastic modulus (Ref 1), and easy to process (Ref 2, 3). However, magnesium is difficult to plastically deform at ambient temperature because it has a hexagonal close-packed (hcp) structure and only basal slip systems get activated to consequence its deformation. The addition of lithium increases the ductility of the Mg-based alloys and further enhances strength-to-weight ratio which allows designers to use thinner sections and achieve an even lower weight for a component. Unfortunately, as the Li content is increased more than 5 wt.%, the mechanical properties are degraded by the formation of a comparatively softer bcc  $\beta$ -phase (Ref 4, 5). Additionally, the Mg-Li alloys have the disadvantage of poor corrosion resistance since the Li atoms are greatly more active than Mg. Consequently, mechanical properties and corrosion resistance of Mg-Li alloy need to be improved. Previous researches on Mg-Li-based alloys have focused mainly on their mechanical properties and development of surface protective coatings (Ref 6-9). Corrosion study of binary Mg-Li alloy has been reported (Ref 6, 10), whereas corrosion mechanism study of multiphase Mg-Li-Al-based alloys has been paid little attention. The elemental composition of the alloy influences the corrosion

properties markedly; small amount (ppm range) of Fe/Ni/Cu may heavily diminish the corrosion resistance of Mg-based alloys (Ref 11). These alloys readily form galvanic corrosion couple with another metal and even a micro-galvanic corrosion system with some secondary phases and /or impurities will correspondingly form in an aqueous environment. Moreover, lithium has even lower standard electrode potential ( $-3.02$  V) compared to magnesium ( $-2.37$  V) (Ref 12), and therefore, alloying with lithium can deteriorate the corrosion resistance of magnesium substrate further. It is thus demanding to improve the corrosion resistance of Mg-Li alloys.

For the development of enhanced corrosion-resistant Mg-Li-based alloys with high strength, additional alloying elements should be added into the alloys. Addition of alloying elements such as Al, Zn, rare earth elements (RE), and Sn enhances the mechanical strength of Mg-Li alloys by solid solution strengthening and precipitation hardening, while improving corrosion resistance. Al and Zn are the most common alloying elements, whereas rare earth elements are commonly added to improve the thermal stability of Mg-Li-based alloys by forming high melting point intermetallic phases. Sn as an alloying element, which is cost effective compared to rare earth elements, can increase the strength by solution strengthening and aging, and also forms the high melting point  $Mg_2Sn$  phase (1043 K) (Ref 13). Corrosion behavior of magnesium and its alloys is different from most other metals such as Fe, Zn, and Cu, because they exhibit the negative difference effect (NDE), which plays a very important role in the process of magnesium corrosion. It is seen experimentally that, when the anodic overvoltage increases, the cathodic release of hydrogen increases rather than decreases (Ref 11). Inferior corrosion resistance is one of the main concerns for the wide industrial application of Mg-Li-based alloys, and a very few studies have been reported on the corrosion study of binary Mg-Li alloys (Ref 10). In addition, Mg-Li-Al-based alloys generally contain significant amounts of second-phase particles (Ref 13). Therefore, local galvanic cells, between the  $\alpha$ -phase- $\beta$ -phases-second-phase particles, form readily on the metal surface in aqueous environments because of the difference in their electrochemical activity. Systematic study of electrochemical behavior of multi-component

**Vinod Kumar**, Department of Metallurgical and Materials Engineering, Malaviya National Institute of Technology Jaipur, Jaipur 302017, India and Materials Research Centre, Malaviya National Institute of Technology Jaipur, Jaipur 302017, India; and **Rajiv Shekhar** and **Kantesh Balani**, Department of Materials Science and Engineering, Indian Institute of Technology Kanpur, Kanpur 208016, India. Contact e-mail: vkt.mnit@gmail.com.

Mg-Li-based alloys, its corrosion mechanism, and their correlation with microstructure is still not very much clear. Therefore, very early stage of corrosion study of lightweight Mg-Li-Al-based alloy has great scientific as well as technological importance, and finding the correct corrosion mechanism thereof might lead to progress in corrosion research of magnesium-lithium-based system.

## 2. Experimental Details

Mg-9Li-7Al-1Sn (LAT971) and Mg-9Li-5Al-3Sn-1Zn (LATZ9531) alloys were melted in a capped stainless steel crucible in an induction furnace and cast in a mild steel mold under a protective atmosphere of argon and sulfur dioxide. After casting, both alloys were annealed at 573 K for 5 h in an argon atmosphere followed by air cooling. Both alloys (12-mm thick) were then thermomechanically (TM) processed in air at  $\sim 573$  K to achieve an approximately 2-mm-thin sheet through sixteen consecutive rolling passes. Before each pass, samples were heated at  $\sim 573$  K for 40 min to relieve the strain introduced due to rolling. The final dimension of the rolled sheets was  $\sim 100 \times 100 \times 2$  mm<sup>3</sup>. TM processed samples of LAT971 and LATZ9531 are hereafter denoted as LAT971R and LATZ9531R, respectively. Further details of processing parameters and characterization of two novel Mg-Li-Al-based alloys namely Mg-9Li-7Al-1Sn (LAT971R) and Mg-9Li-5Al-3Sn-1Zn (LATZ9531R) have also been reported previously (Ref 13-15). A quantitative x-ray wavelength dispersive spectroscopy (WDS) system attached to the EPMA was used to determine the elemental distribution of Mg, Al, Sn, Zn, and minute impurities such as Fe, Ni, and Cu present in LAT971R and LATZ9531R. Corrosion rate was determined by hydrogen gas evolution measurement and electrochemical Tafel extrapolation method. The surface morphology study was performed by utilizing scanning electron microscope (SEM). Mg-3Al-1Zn (AZ31B) alloy has been used for comparison purpose.

### 2.1 Hydrogen Evolution Measurement

All samples were cold mounted at room temperature and ground using standard metallographic procedures and finally polished using 1- $\mu$ m diamond slurry. The funnel and burette of 100 mL capacity were joined with the help of glass blowing unit. The funnel and burette were connected with the help of glass blowing unit and are placed centrally in the beaker with the help of a standing clip. The schematic of experiential arrangement for hydrogen evolution measurement is shown somewhere else (Ref 14). The cold mounted specimens were kept in a beaker, to expose the top polished surface, and then this was filled with 700 mL of electrolyte. The cold mounted polished specimens were kept in a beaker, and then this was filled with 3.5 wt.% NaCl solution.

The temperature of the medium was  $27 \pm 2$  °C. The exposed area for each test was between 1 and 1.5 cm<sup>2</sup>. The atmospheric gas present in upper portion of burette was evacuated manually. The hydrogen gas was collected at the top portion of the burette and then electrolyte was pushed down automatically, as beaker was open to facilitate free aeration. The displaced electrolyte volume represents the volume of hydrogen gas evolved. Typical undergraduate chemistry test was also performed in each case to confirm the evolved gas as hydrogen. Popping

sound was observed when lightening match was approached to the test tube containing the evolved gas which is confirmatory test for the hydrogen gas.

Song and Atrons have reviewed the corrosion rate determination of various Mg-based alloys (excluding Mg-Li-based alloys) from weight loss and hydrogen evolution (Ref 11, 16). It has been concluded that these data were within an error of  $\sim \pm 10\%$  (Ref 12). Therefore, the hydrogen gas evolution tests were also carried out for more than 30 h, in 0.6 M NaCl solution of pH 7.5, to determine the corrosion rate of LAT971R and LATZ9531R alloys. Slight increase in pH (up to pH  $\sim 8.5$ ) was observed after hydrogen gas evolution test experiments.

The simplest and most fundamental measurement of the corrosion rate is the metal weight loss rate,  $\Delta W$  (mg/cm<sup>2</sup>/day). This can be converted to an average corrosion rate,  $P_w$  (mm/year), using following relation

$$P_w = 3.65 \Delta W / \rho, \quad (\text{Eq 1})$$

where  $\rho$  is the metal density (g/cm<sup>3</sup>).

In the overall corrosion reaction of pure Mg, one molecule of hydrogen (i.e., H<sub>2</sub>) is evolved for each atom of corroded Mg. One mole (i.e., 24.31 g) of Mg metal corrodes for each mole (i.e., 22.4 L) of hydrogen gas produced at 273 K and 1 atm. pressure. Therefore, the hydrogen evolution rate,  $V_H$  (mL/cm<sup>2</sup>/day), is related to the metallic weight loss rate,  $\Delta W_m$  (mg/cm<sup>2</sup>/day), at room temperature and 1 atm. pressure, using

$$\Delta W = 1.085 V_H. \quad (\text{Eq 2a})$$

The corresponding corrosion rate,  $P_H$ , is evaluated by substituting Eq 2a into Eq 1 to give

$$P_H = 3.96 V_H / \rho. \quad (\text{Eq 2b})$$

As per the ASTM standard, minimum ratio of 100-200 L/m<sup>2</sup> of exposed area of specimen is usually recommended, in weight loss study, to avoid depletion of corrosive ingredients in the solution. There is no ASTM standard reported for hydrogen evolution measurement. However, the ratio of electrolyte volume to exposed surface area of specimen was maintained at more than 450 L/m<sup>2</sup>. For each experiment, fresh solutions were used and all parts of the experimental set-up were cleaned by acetone.

### 2.2 Electrochemical Polarization

In the present study, the ratio of electrolyte volume to exposed surface area of specimen was maintained at more than 225 L/m<sup>2</sup>. Prior to the experiments, the variation of open-circuit potential (OCP) with time was monitored for one hour. The stabilized OCP was used to define the range of potential for the electrochemical polarization experiments. The standard calomel electrode (SCE) in saturated KCl was used as reference electrode and the counter electrode was a high purity platinum grid. The potential of the reference electrode was +244 mV with respect to standard hydrogen electrode (SHE). The potential of the working electrode was monitored using a SCE. The delay in starting the experiment was minimized by providing connection to the specimen as quickly as possible. The corrosion potential of the working electrode was continuously recorded starting immediately until a steady potential was attained. All the Tafel polarization experiments were begun after stabilization of OCP for 1 h.

Tafel polarization experiments were performed in 0.6 M (3.5 wt.%) of NaCl solution (sea water condition).

Square-shaped specimens of size 1.3 cm × 1.3 cm × 0.2 cm were used for the polarization tests. All specimens were polished with 1200-grit SiC paper and cleaned, according to the ASTM G1-90 standard, using acetone prior to all the tests. The electrochemical polarization experiments were performed using a flat cell and a potentiostat interfaced to a personal computer. The potentiostat used in the present study was PARSTAT 2263 (Princeton Applied Research, USA). A standard electrochemical flat cell of 270 mL capacity was used for all the electrochemical experiments.

The scanning range was from ± 250 mV versus OCP and the scan rate was 0.166 mV/S (Ref 17). The corrosion current densities ( $i_{\text{corr}}$ ) were calculated from the Tafel plots by the Tafel extrapolation method. In the Tafel portion of the curves, maximum possible linearity was maintained during extrapolation. All the experiments were triplicated so as to ensure reproducibility of the test results.

In the Tafel extrapolation method for measuring the corrosion rate of Mg-Li-Al-based alloys, the corrosion current density,  $i_{\text{corr}}$  (mA/cm<sup>2</sup>), is estimated by Tafel extrapolation of the cathodic branch of the polarization curve, and  $i_{\text{corr}}$  is related to the average corrosion rate ( $P_i$ ) in mm/year using following standard equation (Ref 16):

$$P_i = 22.85 i_{\text{corr}} \quad (\text{Eq 3})$$

Corrosion rate obtained for Mg-Li-Al-based alloys by potentiodynamic method was compared and discussed with that obtained by hydrogen evolution method.

### 2.3 Surface Morphology Study

An SEM (Zeiss Model EVO 50, operated at 5-15 kV) with energy dispersive spectroscopy (EDS) (INCA model) was utilized to characterize the surface morphology of both LAT971R and LATZ9531R alloys. The samples were first mechanically polished by emery paper and then successively polished to 1- $\mu\text{m}$  diamond slurry. It was not possible to study the early stage corrosion study of Mg-Li-Al-based alloys in 0.6 M NaCl solution due to very high corrosion rate. Therefore, to develop an early stage corrosion mechanism, corrosion morphology study after 20, 60, 300, 1200, and 3600 s was carried out in very low chloride concentration aerated environment, i.e., 0.01 M NaCl solution (pH ~7.5). After the immersion, the samples were taken out of the solution and rinsed with de-ionized water and acetone to observe the surface morphology of corrosion product. Further, to reveal the effect of chloride ions on the various phases present in Mg-Li-Al-based alloys in chloride solution, the samples were kept for 2 min into boiling chromic acid solution to remove the corrosion product. The samples were then rinsed with de-ionized water and acetone followed by drying in hot air. Surface morphology was studied using back-scattered electrons (BSE) mode in SEM. This study is essential to understand the complete corrosion mechanism of multiphase Mg-Li-Al-based alloys.

## 3. Results and Discussion

Typical SEM images of thermomechanically processed LAT971R and LATZ9531R alloys are shown in Fig. 1(a) and (b), respectively. These micrographs are captured before

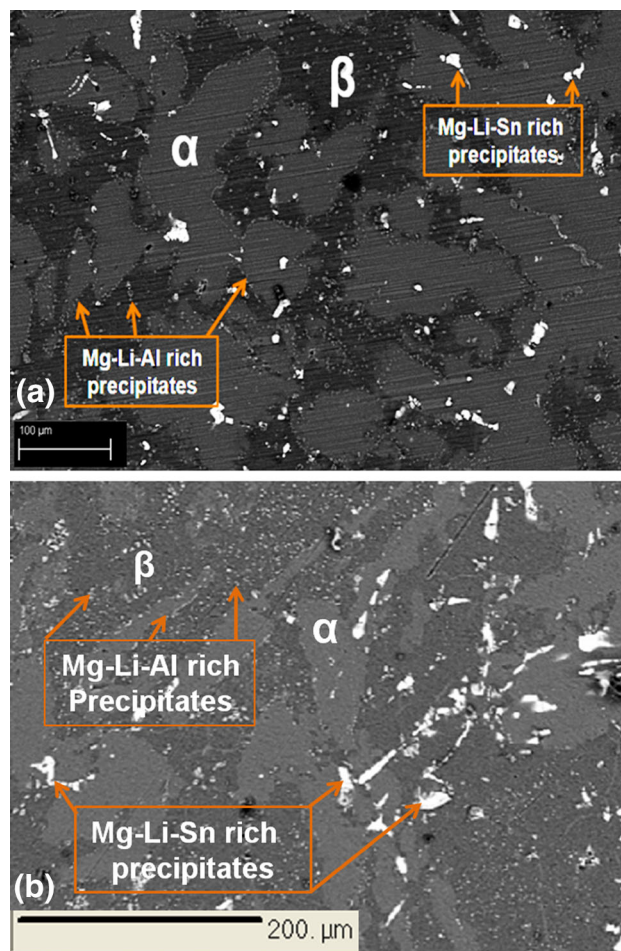


**Fig. 1** (a) Typical SEM image of thermomechanically processed LAT971R before immersion in 0.01 M NaCl solution, (b) Typical SEM image of LATZ9531R (before immersion in 0.01 M NaCl solution)

immersion in 0.01 M NaCl solution. LAT971R and LATZ9531R mainly consist of hcp  $\alpha$ , bcc  $\beta$ , primary precipitate (PP), and secondary precipitates (SP).

Table 1 presents the elemental composition of major phases, i.e., hcp  $\alpha$  and bcc  $\beta$  phases present in LAT971R and LATZ9531R alloys. It is also remarkable to note that the concentrations of Mg, Al, and Zn are higher and the concentration of Li is lower in LATZ9531R compared to that of LAT971R. This trend was observed in case of both major phases, i.e.,  $\alpha$  and  $\beta$ . The detailed EPMA analyses of LAT971R and LATZ9531R confirmed that the primary (coarse) and secondary (fine) precipitates exist as (Mg, Li, Sn) and (Mg, Li, Al) phases, respectively, and all the phases present in both alloys are almost free from impurity elements such as Fe and Ni. However, it is important to note that Cu ( $0.0125 \pm 0.0088$ ) was present only in secondary precipitates of LAT971R. Two types of precipitates, namely primary precipitates (Mg-Li-Sn-based) and secondary precipitates (Mg-Li-Al-based), were predominantly distributed in  $\alpha$ -phase and  $\beta$ -phase, respectively (Ref 13).

### 3.1 Hydrogen Gas Evolution Measurement

The hydrogen evolution volume (HEV) was measured as a function of immersion time in 0.6 M NaCl for LAT971R,

**Table 1** Composition (mol.%) of  $\alpha$ -phase and  $\beta$ -phase formed in LAT971R and LATZ9531R (Estimated by EPMA analysis)

Alloy	Phase	Mg	Li	Al	Sn	Zn	Others
LAT971R	$\alpha$ -Mg	77.33 $\pm$ 3.78	17.91 $\pm$ 4.24	4.45 $\pm$ 0.43	0.044 $\pm$ 0.077	Nil	0.27
	$\beta$ -Li	65.88 $\pm$ 2.65	32.26 $\pm$ 1.66	1.74 $\pm$ 0.24	0.007 $\pm$ 0.005	Nil	0.11
LATZ9531R	$\alpha$ -Mg	80.27 $\pm$ 1.85	15.31 $\pm$ 2.36	4.28 $\pm$ 1.69	0.038 $\pm$ 0.010	0.081 $\pm$ 0.08	0.021
	$\beta$ -Li	69.23 $\pm$ 2.38	28.52 $\pm$ 1.59	2.13 $\pm$ 0.44	0.000	0.012 $\pm$ 0.05	0.108

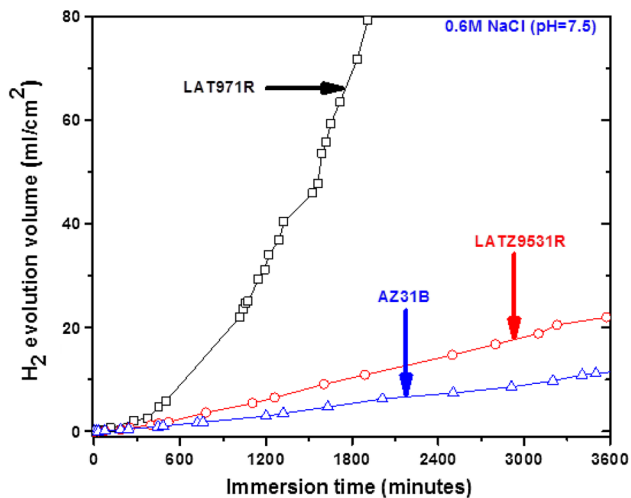


**Fig. 2** Hydrogen evolution volume (mL/cm<sup>2</sup>) as a function of immersion time for LAT971R, LATZ9531R, and AZ31B in 0.6 M NaCl solution at pH 7.5

**Table 2** Cumulative hydrogen evolution rate (mL/cm<sup>2</sup> day) for LAT971R, LATZ9531R, and AZ31B immersed for 30 h in the 0.6 M NaCl solution

Material	pH	1 h	5 h	10 h	20 h	30 h
LAT971R	7.5	16.01	10.92	~16.81	40.17	56.29
LATZ9531R	7.5	4.86	~4.20	~5.05	7.51	8.75
AZ31B	7.5	2.63	~3.06	~3.36	3.59	~4.26

LATZ9531R, and AZ31B at pH 7.5 to determine the corrosion rate of these alloys and the results of which are presented in Fig. 2. Slight increase in pH (up to pH ~8.2-8.5) was observed after hydrogen gas evolution test experiments which may be due to high ratio of electrolyte volume to exposed surface area of specimen, i.e., 450 L/m<sup>2</sup>.

The hydrogen evolution rates (mL/cm<sup>2</sup> day) of LAT971R, LATZ9531R, and AZ31B averaged over 1, 10, 20, and 30 h of immersion time in 0.6 M NaCl are summarized in Table 2. Here it is observed that at pH 7.5-8.5, the average corrosion rate of LAT971R increases more than 2.5 times when averaging period is increased beyond 10 h. The corresponding increase in LATZ9531R is much less. AZ31B was relatively much more corrosion resistant than either LAT971R or LATZ9531R. Here, it can be seen that HEV can be ranked in an increasing order as AZ31B < LATZ9531R < LAT971R. The higher rate of hydrogen gas evolution in case of both alloys, i.e., LAT971R and LATZ9531R, compared to AZ31B is mainly due to the presence of higher Li content present in both Mg-Li-Al-based

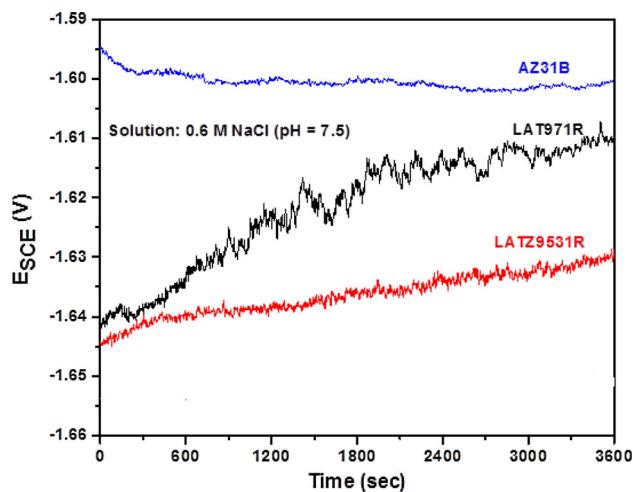


**Fig. 3** Variation of free corrosion potential as function of immersion time for LAT971R, LATZ9531R, and AZ31B in 0.6 M NaCl solution

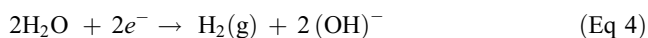
alloys. However, LATZ9531R has lower HEV compared to that of LAT971R which may be due to the presence of even more amount of Li in its major phases, i.e.,  $\alpha$  and  $\beta$ . In addition, the presence of about 125 ppm of Cu in secondary precipitates of LAT971R makes it more prone to form strong micro-galvanic cells between secondary precipitates and  $\beta$ -phase. The high amount of Cu present in secondary precipitates, which is distributed in  $\beta$ -phase of LAT971R, is also responsible for higher HEV.

### 3.2 Electrochemical Test

The variation of open-circuit potential (OCP) measured as function of time for LAT971R, LATZ9531R, and AZ31B alloys in 0.6 M concentration NaCl solution is shown in Fig. 3, from where it is noted that AZ31B stabilized at more noble potentials compared to LAT971R and LATZ9531R. The change in OCP with time up to 3600 s was not significant.

Typical polarization curves of LAT971R, LATZ9531R, and AZ31B in 0.6 M NaCl solution of pH 7.5 are presented in Fig. 4. This shows that the anodic polarization curves for both LAT971R and LATZ9531R are roughly the same. However, the hydrogen evolution (cathodic) reaction is least polarized in LAT971R. This phenomenon is reflected in Table 3 which shows that  $i_{\text{corr}}$  is highest in LAT971R. The corrosion rate of these Mg-Li-Al-based alloys, in 0.6 M NaCl solutions, in mm/year can be arranged in the following order: AZ31B < LATZ9531R < LAT971R. In a slightly basic (pH ~7.5) aqueous medium, cathodic reaction, i.e., hydrogen evolution,

will follow Eq 4. The related half-cell reaction in 0.6 M NaCl solution is supposed to be as follows (Ref 14):



Song and other researchers (Ref 10) reported that the anodic reactions are mainly due to magnesium dissolution only in case of binary Mg-Li alloys according to Eq 5a and 5b. The nature of the anodic parts of AZ31B, LAT971, and LATZ9531 alloys (see Fig. 4) clearly revealed that the anodic reaction is not controlled by magnesium dissolution only. It is interesting to note that high amount of lithium, even more than 25 vol.%, is present in case of both LAT971 and LATZ9531 alloys and lithium has negatively higher reduction potential compared to magnesium. Therefore, it is speculated that extra anodic dissolution of lithium also occurs simultaneously along with the dissolution of magnesium and hydrogen evolution. Hence, it can be concluded that lithium dissolution is also a part of overall anodic reaction as per Eq 6. Anodic dissolution reactions may be combination of Eq 5a, 5b, and 6.



The reaction of  $\text{Mg}^+$  with water to produce hydrogen gas is in doubt (Ref 18, 19) which is reported by one group of researcher (Ref 10) and this needs to be further investigated. Hence, further advanced study is required to establish the reaction of  $\text{Mg}^+$  with water in case of LAT971R and LATZ9531R alloys. Furthermore, the potential sites for dissolution reaction and hydrogen evolution were identified by studying the hydrogen bubble study in optical microscope, which is discussed in detail later.

### 3.3 Comparison of Hydrogen Evolution and Tafel Extrapolation Results

The corrosion rate measured for LAT971R, LATZ9531R, and AZ31B in 0.6 M NaCl solution with pH 7.5 by hydrogen evolution measurement,  $P_H$ , is given in Table 4. The corrosion rate values were determined using Eq 3. The data of Table 4 relate to the corrosion rate by hydrogen evolution measurement,  $P_{H1}$ ,  $P_{H10}$ , and  $P_{H30}$ , measured over 1, 10, and 30 h, respectively. The corrosion rate values for these alloys by using Tafel extrapolation data,  $P_i$ , measured after 1 h specimen immersion in the solution are also provided in Table 4 for the comparison purpose.

The observed  $P_{H1}$ ,  $P_{H10}$ , and  $P_{H30}$  values are larger than expected for all the samples in the same solution as determined using Tafel extrapolation parameter, which is evident by a comparison of the data provided in Table 4. The ratio of corrosion rate values determined by hydrogen evolution measurement to that of by the Tafel curves varies between 2.53 and 9.69. These large ratio values are in agreement with the observations of the corrosion study of other reported mainly Mg-Al-based alloys (Ref 16). The ratio ( $P_{H30}/P_i$ ) became larger when the specimen was immersed for longer time. This confirmed that the corrosion product forming on the sample surface is not protective in nature, and these larger values of  $P_{H30}/P_i$  also indicate that there was not good agreement

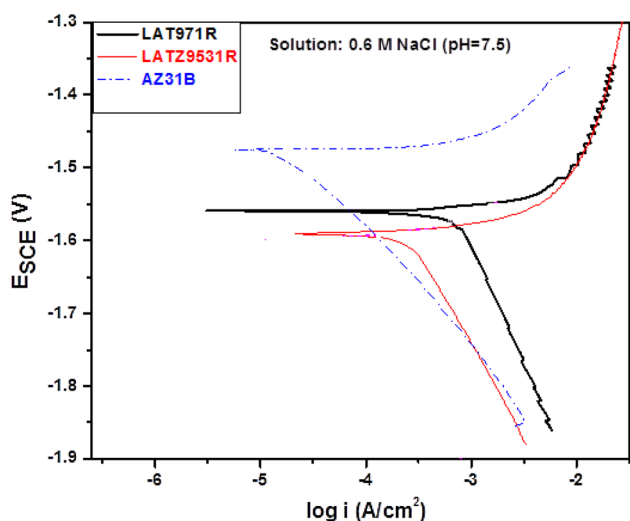


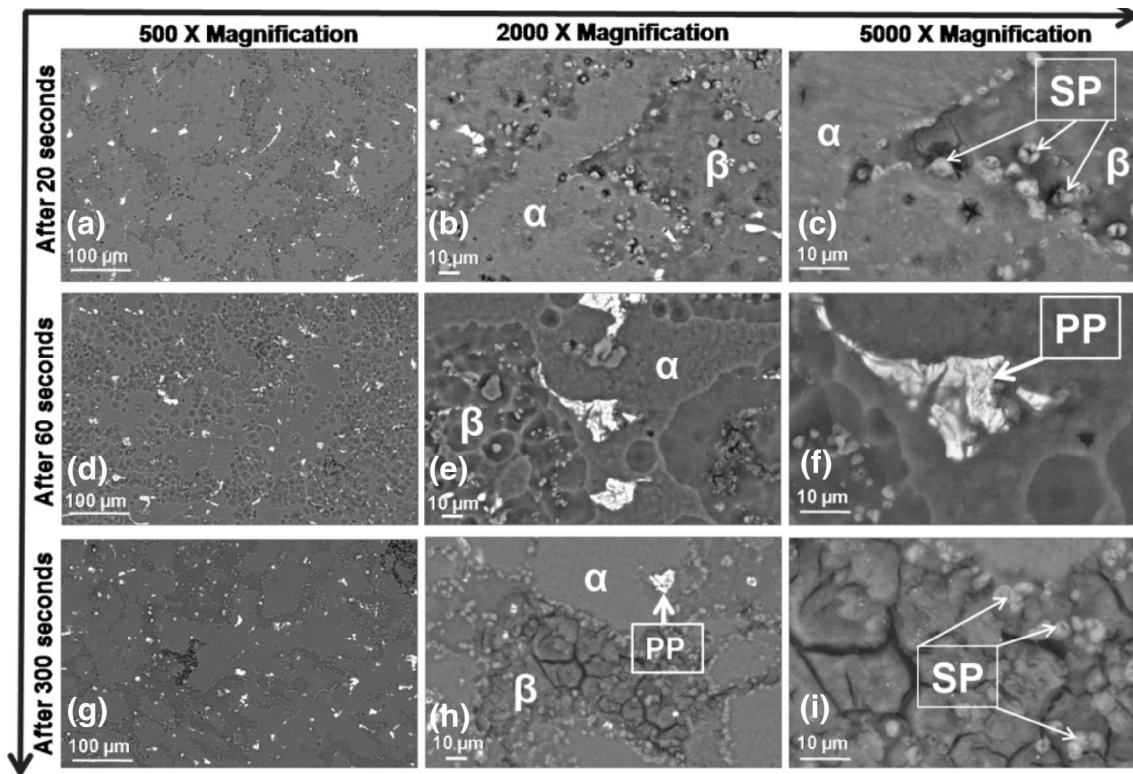
Fig. 4 Polarization curves for LAT971R, LATZ9531R, and AZ31B in 0.6 M NaCl solution with pH 7.5

Table 3 Fitting results of polarization curve for LAT971R, LATZ9531R, and AZ31B in 0.6 M NaCl solution with pH 7.5

Sample	OCP, V	$E_{\text{corr}}$ , V	$i_{\text{corr}}$ , mA/cm <sup>2</sup>	Corrosion rate, $P_i$ (mm/year) = 22.85 $i_{\text{corr}}$
LAT971R	-1.61	-1.56	0.654	14.94
LATZ9531R	-1.63	-1.59	0.216	4.94
AZ31B	-1.60	-1.47	0.054	1.23

Table 4 Comparison of corrosion rates (mm/year) for LAT971R, LATZ9531R, and AZ31B, measured by hydrogen evolution test,  $P_H$  ( $\sim 2.571 \cdot \text{HER}$ ) for more than 30 h immersion in 0.6 M NaCl (pH 7.5); and  $P_i$ , evaluated by Tafel extrapolation

Samples	$i_{\text{corr}}$ , mA/cm <sup>2</sup>	$P_i$ , mm/year	$P_{H1}$ , mm/year	$P_{H10}$ , mm/year	$P_{H30}$ , mm/year	$P_{H1}/P_i$	$P_{H10}/P_i$	$P_{H30}/P_i$
LAT971R	0.654	14.94	41.16	43.22	144.72	2.76	2.89	9.69
LATZ9531R	0.216	4.94	12.49	12.98	22.49	2.53	2.63	4.55
AZ31B	0.054	1.23	6.76	8.64	10.95	5.48	7.00	8.87



**Fig. 5** Ex situ SEM images, at different magnifications, showing the microstructure evolution of LAT971R at immersion times of (a) 20 s, (b) 60 s, and (c) 300 s in 0.01 M NaCl

between the corrosion rates, calculated by hydrogen evolution and by Tafel extrapolation.

There are four assumptions taken to determine corrosion rate by polarization method, namely (i) a single anodic and cathodic reaction exists for the electrode under study, (ii) electrode surface does not change during polarization, (iii) at a given scan rate, the electrode reactions reach equilibrium at every value of applied potential, and (iv) corrosion current density is uniform over the entire surface. It was observed that these assumptions do not apply well in the case of the present samples under study, i.e., LAT971R and LATZ9531R. Song et al. (Ref 20) have proposed that there are at least three reactions occurring on the magnesium surface immersed in solution in case of binary Mg-Li-based alloy: dissolution of magnesium metal and hydrogen evolution as anodic reaction and separate hydrogen evolution as cathodic reaction. The negative difference effect, associated with the anodic hydrogen evolution, results in higher dissolution rate of magnesium at every applied anodic over potentials. In case of LAT971R and LATZ9531R alloys, the amount of lithium (which has negatively higher reduction potential compared to magnesium) is more than 25 vol.%, so extra anodic dissolution of lithium also expected to occur. As a result, there is minimum four reactions, in accordance with Eq 4 to 7, occurring simultaneously on the surface of the Mg-Li-Al-based alloys, such as LAT971R and LATZ9531R. This situation violates the first assumption.

The increase in OCP value with immersion time indicated the incessant formation of corrosion film on the surface. In this manner, the second assumption is violated. For a chosen scan rate of the value 0.166 mV/s, it is speculated that equilibrium condition may not achieved due to the presence of multiphase

structure in LAT971R and LATZ9531R and this will lead to non-uniform current density over the specimen surface. Therefore, the third and fourth of the above said assumption are also violated. This restricts the application of polarization curve for the corrosion rate determination of LAT971R and LATZ9531R. The above discussion suggests that there is severe problem with the normal electrochemical method for corrosion rate determination of Mg-Li-Al-based alloys too. It can be concluded that the corrosion rate determination of alloys containing Mg and Li will give more reliable results if determined via hydrogen gas evolution test rather than the Tafel extrapolation method. Further study can focus on developing an appropriate model for determining the corrosion rate of Mg-Li-Al-based alloys by electrochemical methods.

### 3.4 Surface Morphology Evolution

Present surface morphology evolution study is to develop the basic understanding about the corrosion mechanism in Mg-Li-Al-based multiphase alloys. In continuation to this, the results of corrosion morphology study after 20, 60, 300, 1200, and 3600 s were carried out in very low chloride concentration aerated environment, i.e., 0.01 M NaCl solution with pH 7.5.

Figure 1(a) shows the dual-phase ( $\alpha + \beta$ ) structure of LAT971R along with the Mg-Li-Sn-rich primary precipitates and the Mg-Li-Al-rich secondary precipitates. Figure 5 shows the surface morphology of LAT971R after 20, 60, and 300 s at three different magnifications. After 20 s of immersion in solution, pits, manifested by dark regions, were primarily observed around the secondary precipitates, as shown in Fig. 5(b) and (c). At very early stage of immersion, initiation

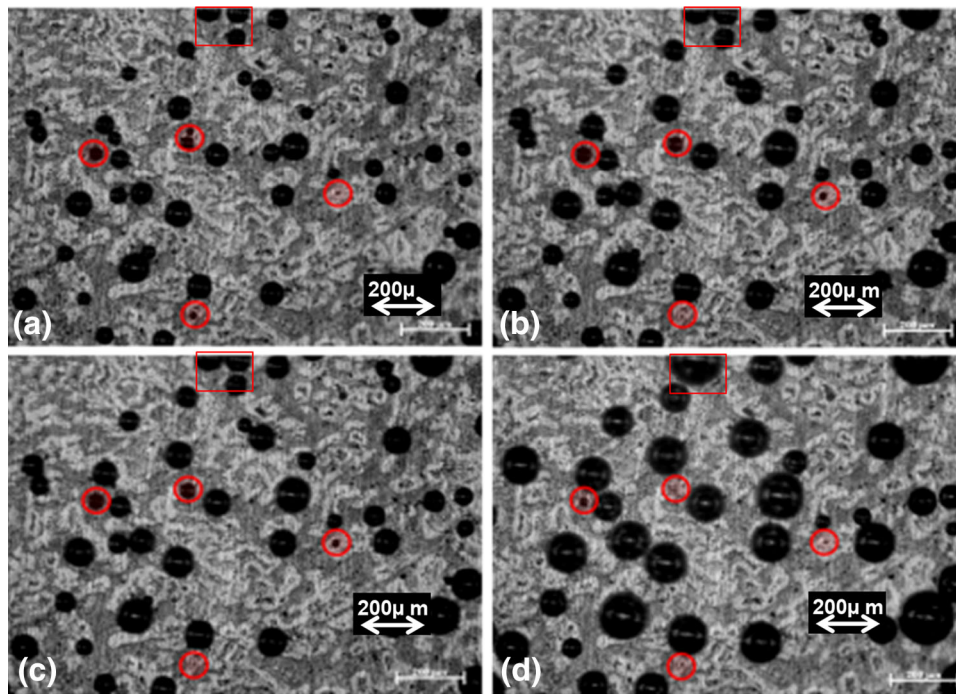


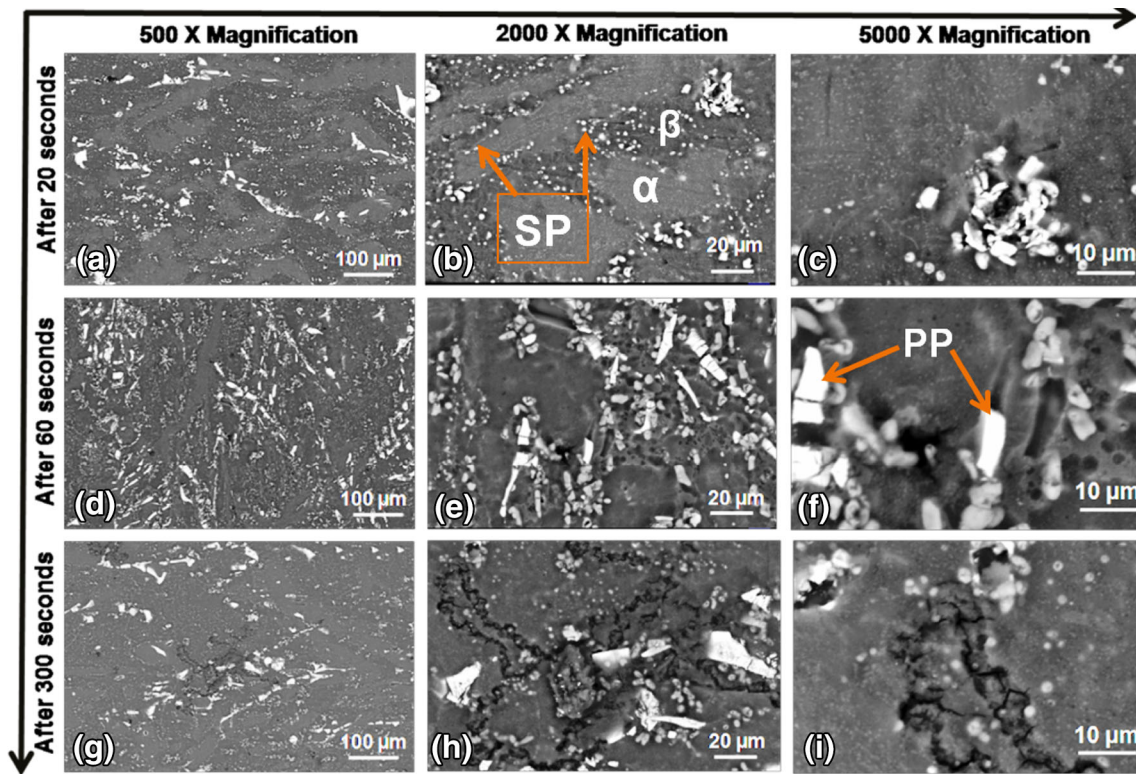
**Fig. 6** Optical micrographs showing hydrogen bubble evolution, combination, and bursting on the surface of Mg-Li-Al-based alloys after (a) 20 s, (b) 30 s, (c) 45 s, and (d) 60 s, when immersion in 0.01 M NaCl solution

of pits was observed only around secondary precipitates. In this condition after immersion, the SP phase remained in the structure while  $\beta$ -phase around was corroded and almost disappeared; hence, in LAT971R alloy, the SP phase acts as the cathode and  $\beta$ -phase plays the local anode role. Therefore,  $\beta$ -phase cannot further support the SP phase and pit formed. Here, it is worth noting that difference in chemical composition as a result of high amount of alloying elements such as Cu (125 ppm), Al, etc. present in some of SPs and high amount of Li present in  $\beta$ -phase leads to the formation of strong microgalvanic couple between them which is the driving force for pit formation around secondary precipitates. After 60 s, the increasing dissolution of the native oxide film is evident when the size of the “cavity” around the secondary precipitates in Fig. 5(e) and (f) is compared with the size of the pits in Fig. 5(b) and (c), respectively. In all probability, the size of the pits must have also increased with immersion time from 20 to 60 s. The smooth texture of the  $\alpha$  phase after 300 s in Fig. 5(h), when compared to Fig. 5(b) and (d), suggests that the natural oxide film covering on it has dissolved completely. At this time, the corrosion initiated in the form of pits has progressed as intergranular corrosion in the  $\beta$  phase (see Fig. 5h and i). Moreover, the surface morphology in Fig. 5(i) and the smooth texture of the  $\alpha$  phase, as seen in Fig. 5(h), suggest that the corrosion product, that is the hydroxide film, has started depositing preferentially on the  $\beta$  phase. Furthermore, the area around the primary precipitates appears to be unaffected by corrosion even after 300 s. It is also possible that hydroxide formation may have initiated on the  $\alpha$  phase due to hydrolysis of the oxide film (Ref 10). Liu et al. (Ref 21) and Ha et al. (Ref 22) have reported that  $Mg_2Sn$  precipitates may be responsible for pitting in Mg-Sn-based alloys. However, morphology study of Mg-Li-Al-based alloys revealed that Mg-Li-Sn-based precipitates (PP) were forming the continuous film with matrix.

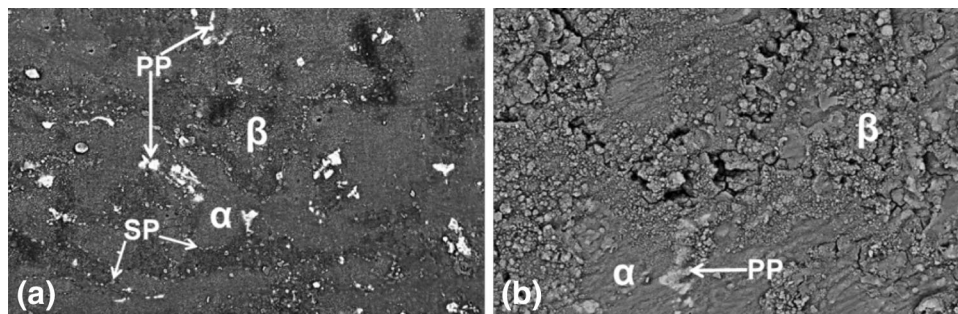
This may be either due to similar electrode potential between primary precipitate and  $\alpha$ -phase, or stable oxide formed on these precipitates, which is immune to 0.01 M NaCl solution.

Figure 6 shows in situ optical micrographs of hydrogen bubbles generated on LAT971R after 20, 30, 45, and 60 s. The location and evolution of the size of hydrogen bubbles shed light on the dynamics of corrosion. Figure 6(a) shows the random generation of hydrogen bubbles, which is consistent with the earlier observation that corrosion is initiated randomly at sites where the native oxide layer has been removed by  $Cl^-$ . Figure 6(a) to (d) shows that the size of the hydrogen bubble increases with time, in general, but in some locations marked by “red circles,” the bubble size decreases with time. Increase in the size of hydrogen bubbles with time suggests an increase in the extent of pitting corrosion. For example, three separate bubbles, enclosed in a rectangle, at the top center of Fig. 6(a) join after 60 s, which indicates that three distinct pits have merged together. On the other hand, the reduction in the bubble size with time can be correlated with the formation of protective corrosion product, which restricts the reaction of electrolyte ions with the surface of the LAT971R and LATZ9531R samples. Consequently, Fig. 6 substantiates the conclusions drawn from Fig. 5. It further suggests that the formation of the protective hydroxide layer starts as early as 30 s after immersion in NaCl.

Figure 7 shows the evolution of microstructure in case of multiphase structure of LATZ9531R after immersion in 0.01 M NaCl. It has been reported that the proportion of precipitates is higher in LATZ9531R ( $\sim 10\%$ ) compared to LAT971R ( $\sim 3\%$ ) (Ref 11). However, a comparison of Fig. 6 and 7 shows that the surface morphology evolution in LATZ9531R is similar to that in LAT971R. A careful examination of Fig. 7(c) shows the presence of a third type of extremely fine precipitates, which are present in both  $\alpha$  and  $\beta$  phases. It may be pointed out that



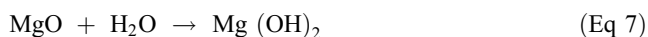
**Fig. 7** Ex situ SEM images, at different magnifications, showing the microstructure evolution of LATZ9531R at immersion times of (a) 20 s, (b) 60 s, and (c) 300 s in 0.01 M NaCl



**Fig. 8** Typical back-scattered SEM image of LAT971 showing surface morphology of LAT971 exposed in 0.01 M NaCl solution after: (a) 1200 s and (b) 3600 s

the fine precipitates were visible only after immersion in NaCl for 20 s (Ref 14). These fine precipitates can also be observed in LAT971 (see Fig. 5c). Fig. 8 shows that the surface of LAT971 is covered by a mixed hydroxide film after 1200 and 3600 s. However, the film covering the  $\alpha$  phase is more compact. Fig. 9 shows the nature of the hydroxide film in LATZ9531. Here a cotton ball type of hydroxide morphology was observed over alpha and beta phases.

The mixed hydroxide films,  $\text{Mg}(\text{OH})_2$  and  $\text{Li}(\text{OH})$ , were formed according to Eq 7 and 8 (Ref 10). Song et al. have reported that mixed hydroxide film was formed on binary Mg-8Li alloy after 7200 s of immersion in 0.1 M NaCl solution (Ref 10).



This observation is unique in this aspect because Song et al. (Ref 10) have studied surface morphology study of binary Mg-Li alloy extensively for 2-24 h of immersion, and early stage observation is missing for this class of materials. On the basis of the present study, it can be concluded that mixed hydroxide film formed on the surface of the present Mg-Li-Al-based alloys even after  $\sim 1200$  s only, as shown in Fig. 8 and 9.

In order to reveal the morphology of corrosion attack on the LAT971R and LATZ9531 alloys, the corrosion product was removed from the surface, prior to the SEM analysis. This was accomplished by immersing the corroded samples in a boiling solution of 180 g/L chromic acid for two minutes. The corrosion product was removed for the samples, which were immersed for 1200 and 3600 s.



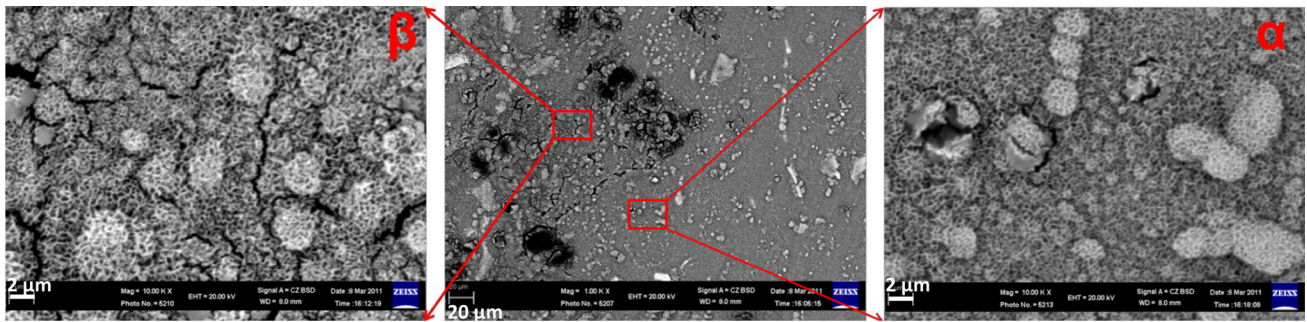


**Fig. 9** Typical cotton ball structure of hydroxide present in LATZ9531R after immersion in 0.01 M NaCl solution for 1200 s

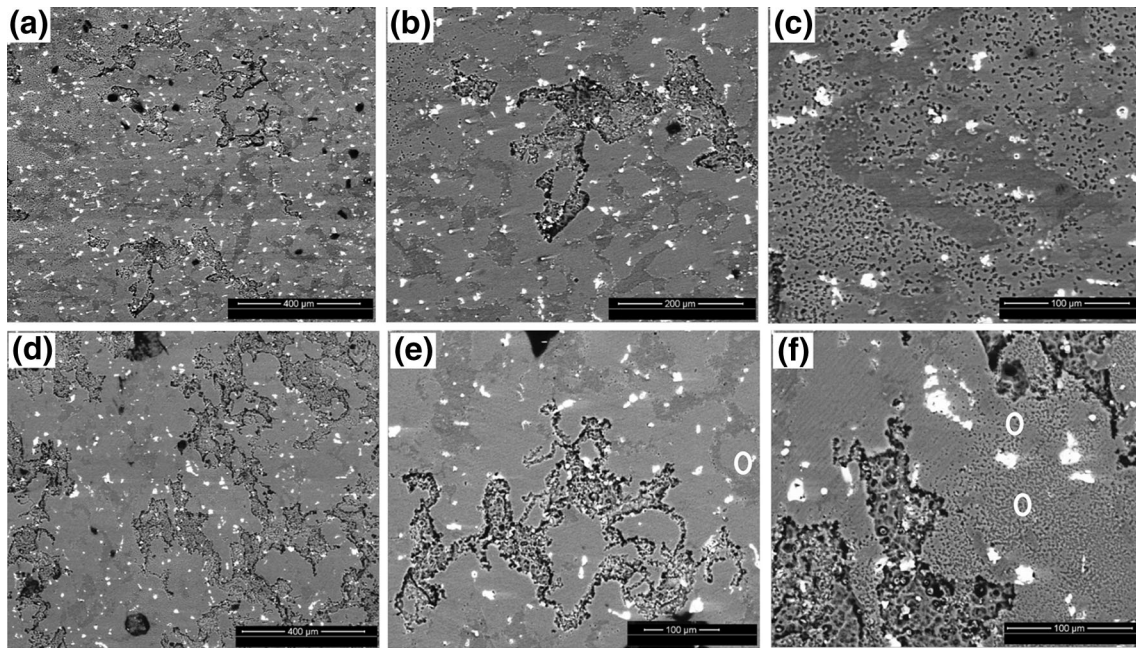


**Fig. 10** Ex situ SEM micrographs of LAT971R surface, after removal of surface layer, as a function of immersion time in 0.01 M NaCl solution: (a), (b) and (c) after 1200 s immersion period and (d), (e) and (f) after 3600 s of immersion. Typical micro-pits are represented by white circle

Ex situ (Post immersion) SEM micrographs in back-scattered electron (BSE) mode for LAT971R and LATZ9531R alloys in 0.01 M NaCl solution after different immersion time intervals are shown in Fig. 10 and 11, respectively. Typical filaments were observed in case of LAT971R (Fig. 10a) and LATZ9531R (Fig. 11a) after 1200 s of immersion. The filaments propagate both in longitudinal and transverse directions (compare Fig. 10a and 11a with 10d and 11d, respectively) with respect to the time of immersion. The SEM micrographs (Fig. 10d-f and 11d-f) revealed that the primary precipitates were not affected and were intact with the matrix even after immersion for 3600 s. It can be seen that the severity of attack also increased with immersion time. Furthermore, Figs. 10(b) and 11(b) also suggest that secondary precipitates present in the  $\beta$ -phase were removed from the matrix because of pit formation. The SEM micrographs (Fig. 10 and 11) further confirmed that LAT971R and LATZ9531R alloys underwent non-uniform corrosion in 0.01 M NaCl solution. Figures 10(f) and 11(f) clearly show the presence of extremely small pits in  $\alpha$  phase, most probably caused by the potential difference

between the extremely small precipitates and the  $\alpha$  matrix. In the  $\beta$  phase, extremely fine precipitates were not clearly visible due to the presence of secondary precipitate generated pits.

It is well established for Mg-based alloys that the  $\alpha$ -phase (anode) always corrodes preferentially and other phases, such as second phases and intermetallic act as cathodes or act as corrosion barrier (Ref 16, 23-25). However, it can be concluded based on the early stage of corrosion study of LAT971R and LATZ9531R that (i)  $\alpha$ -phase (cathode) does not corrode preferentially due to the presence of high amount of Al, Zn, and Sn in solution (Ref 22) and comparatively low Li in solid solution of  $\alpha$ -phase; (ii) precipitates or intermetallic, i.e., primary precipitates (Mg-Li-Sn-rich) do not act as cathode when it is distributed in  $\alpha$ -phase which may be due to their comparable electrode potential values; (iii) precipitates act either as anode or cathode depending on the chemistry of the precipitates, their surrounding phase, and its electrode potential value compared to matrix phase. Based on the present study, it can be concluded that present multiphase Mg-Li-Al-based alloys are exception in this series because of the more active

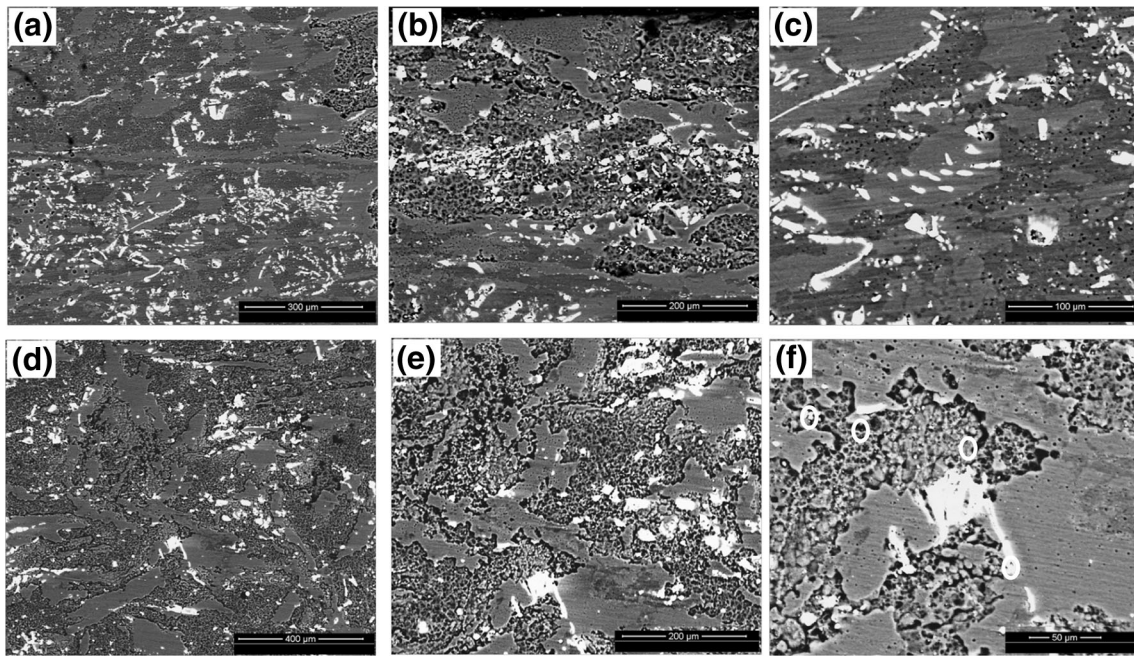


**Fig. 11** Ex situ SEM micrographs of LATZ9531R surface, after removal of surface layer, as a function of immersion time in 0.01 M NaCl solution: (a), (b) and (c) after 1200 s immersion period and (d), (e) and (f) after 3600 s of immersion. Typical micro-pits are represented by white circle

nature of  $\beta$ -phase and distinctive chemical composition of both the precipitates. Finally it should be noted that early stage of corrosion behavior of Mg-Li-based alloys is an important and not well-understood research area that demands significant further research and development. The use of advance micro-probe-based electrochemical tools can be utilized which would facilitate better understanding of initial stage of corrosion in Mg-Li-Al-based alloys.

#### 4. Conclusions

1. Corrosion rate determination of two novel Mg-Li-Al-based alloys by hydrogen evolution measurement has revealed different trend in similar conditions when compared to that of the Tafel polarization results.
2. The corrosion rate of LAT971R was reasonably higher compared to LATZ9531R, and both alloys have shown higher corrosion rate compared to AZ31B which is mainly because of chemical inhomogeneity, negative difference effect (NDE), unprotective oxide and/or hydroxide layer on the surface, and the local micro-galvanic activity in the multiphase LAT971R and LATZ9531R alloys.
3. There is severe reliability problem with the normal electrochemical method (Tafel extrapolation) for corrosion rate determination of Mg-Li-Al-based alloys, which can be obviated via hydrogen evolution method because of negative difference effect and the presence of Li.
4. The micro-galvanic corrosion of primary precipitate (PP) and  $\alpha$ -phase is not as severe as was observed in case of the secondary precipitates (SP) and  $\beta$ -phase which corroborated that the chemical composition of the phases and its distribution are the key parameters deciding the

corrosion morphology and its nature in case of Mg-Li-Al-based alloys.

#### Acknowledgment

The authors acknowledge funding from IITK-ISRO cell Project No. MET /ISRO 20090011. VK thanks one of his Ph.D. supervisors Late Prof. R. Balasubramaniam (Professor, Department of Materials Science and Engineering at IIT Kanpur, India) for his help and guidance during the early design of the experiments. The authors would like to thank Mr. Govind (Scientist, ISRO; Trivandrum, India) for his help during sample preparation.

#### References

1. W.A. Counts, M. Friák, D. Raabe, and J. Neugebauer, Using Ab Initio Calculations in Designing bcc Mg-Li Alloys for Ultra-Lightweight Applications, *Acta Mater.*, 2009, **57**, p 69-76
2. O. Sivakesavam and Y.V.R.K. Prasad, Characteristics of Superplasticity Domain in the Processing Map for Hot Working of As-cast Mg-11.5 Li-1.5 Al Alloy, *Mater. Sci. Eng., A*, 2002, **323**, p 270-277
3. X. Liu, G. Du, R. Wu, Z. Niu, and M. Zhang, Deformation and Microstructure Evolution of a High Strain Rate Superplastic Mg-Li-Zn Alloy, *J. Alloy. Compd.*, 2011, **509**, p 9558-9561
4. Z. Drozd, Z. Trojanová, and S. Kúdela, Deformation Behavior of Mg-Li-Al Alloys, *J. Alloy. Compd.*, 2004, **378**, p 192-195
5. X. Meng, R. Wu, M. Zhang, L. Wu, and C. Cui, Microstructures and Properties of Superlight Mg-Li-Al-Zn Wrought Alloys, *J. Alloy. Compd.*, 2009, **486**, p 722-725
6. L. Yang, J. Li, X. Yu, M. Zhang, and X. Huang, Lanthanum-Based Conversion Coating on Mg-8Li Alloy, *Appl. Surf. Sci.*, 2008, **255**, p 2338-2341
7. Y. Ma, N. Li, D. Li, M. Zhang, and X. Huang, Characteristics and Corrosion Studies of Vanadate Conversion Coating Formed on Mg-

- 14 wt% Li–1 wt% Al–0.1 wt% Ce Alloy, *Appl. Surf. Sci.*, 2012, **261**, p 59–67
8. G. Wang, M. Zhang, and R. Wu, Molybdate and Molybdate/Permanganate Conversion Coatings on Mg–8.5 Li Alloy, *Appl. Surf. Sci.*, 2012, **258**, p 2648–2654
  9. P.C. Wang, T.C. Cheng, H.C. Lin, M.J. Chen, K.M. Lin, and M.T. Yeh, Effects of Pre-sputtered Al Interlayer on the Atomic Layer Deposition of Al<sub>2</sub>O<sub>3</sub> Films on Mg–10Li–0.5Zn Alloy, *Appl. Surf. Sci.*, 2013, **270**, p 452–456
  10. Y. Song, D. Shan, R. Chen, and E.-H. Han, Corrosion Characterization of Mg–8Li Alloy in NaCl Solution, *Corros. Sci.*, 2009, **51**, p 1087–1094
  11. G. Song and A. Atrens, Understanding Magnesium Corrosion, *Adv. Eng. Mater.*, 2003, **5**, p 837–858
  12. R.W. Revie, *Uhlig's Corrosion Handbook*, 2nd ed., Wiley, New York, 2000
  13. V. Kumar, R. Shekhar, R. Balasubramaniam, and K. Balani, Microstructure Evolution and Texture Development in Thermomechanically Processed Mg–Li–Al Based Alloys, *Mater. Sci. Eng., A*, 2012, **547**, p 38–50
  14. V. Kumar, Ph.D. Thesis, Materials Science and Engineering, Indian Institute of Technology Kanpur, Kanpur, 2012
  15. V. Kumar, R. Balasubramaniam, R. Shekhar, and K. Balani, Microstructure and Texture Evolution During Hot Rolling of Mg–9Li–7Al–1Sn Alloy for Aerospace Application, *Mater. Sci. Forum*, 2012, **702–703**, p 85–88
  16. Z. Shi, M. Liu, and A. Atrens, Measurement of the Corrosion Rate of Magnesium Alloys Using Tafel Extrapolation, *Corros. Sci.*, 2010, **52**, p 579–588
  17. R.G. Kelly, J.R. Scully, D.W. Shoesmith, and R.G. Buchheit, *Electrochemical Techniques in Corrosion Science and Engineering*, 1st ed., Marcel Dekker Inc., New York, 1999
  18. N.T. Kirkland, G. Williams, and N. Birbilis, Response to Comments from Shi and Atrens on the Paper “Observations of the Galvanostatic Dissolution of Pure Magnesium”, *Corros. Sci.*, 2013, **77**, p 407–409
  19. G. Williams, N. Birbilis, and H.N. McMurray, The Source of Hydrogen Evolved from a Magnesium Anode, *Electrochem. Commun.*, 2013, **36**, p 1–5
  20. G. Song, A. Atrens, D. John, X. Wu, and J. Naim, The Anodic Dissolution of Magnesium in Chloride and Sulphate Solutions, *Corros. Sci.*, 1997, **39**, p 1981–2004
  21. X. Liu, D. Shan, Y. Song, R. Chen, and E. Han, Influences of the Quantity of Mg<sub>2</sub>Sn Phase on the Corrosion Behavior of Mg–7Sn Magnesium Alloy, *Electrochim. Acta*, 2011, **56**, p 2582–2590
  22. H.-Y. Ha, J.-Y. Kang, S.G. Kim, B. Kim, S.S. Park, C.D. Yim, and B.S. You, Influences of Metallurgical Factors on the Corrosion Behaviour of Extruded Binary Mg–Sn Alloys, *Corros. Sci.*, 2014, **82**, p 369–379
  23. A. Froats, T.K. Aune, D. Hawke, W. Unsworth, and G. Hillis, Corrosion of Magnesium and Magnesium Alloys, *Metal Handbook*, 9th ed., L.J. Korb, and D.L. Olson, Ed., ASM International, Materials Park, OH, 1987
  24. E. Ghali, *Corrosion Resistance of Aluminum and Magnesium Alloys—Understanding, Performance and Testing*, Wiley, Hoboken, NJ, 2010
  25. H. Godard, W.B. Jepson, M.R. Bothwell, and R.L. Kane, *The Corrosion of Light Metals*, Wiley, New York, 1967